PAPER

# Effects of anode evaporation process on the anode sheath characteristics in vacuum arc plasma

IOP Publishing Journal of Physics D: Applied Physics
J. Phys. D: Appl. Phys. **58** (2025) 115201 (8pp) https://doi.org/10.1088/1361-6463/ad7c5c

# Effects of anode evaporation process on the anode sheath characteristics in vacuum arc plasma

**Zhaohui Liu[1,2], Mengmeng Song[1,2], Ziming Wang[1,2], Wei Yang[1], Ye Dong[1], Qiang Sun[1,*] and Qianhong Zhou[1,*]**

[1] Institute of Applied Physics and Computational Mathematics, Beijing 100094, People's Republic of China
[2] Graduate School of China Academy of Engineering Physics, Beijing 100088, People's Republic of China

E-mail: sq19992@mail.ustc.edu.cn and zhou_qianhong@qq.com

Received 4 June 2024, revised 22 August 2024
Accepted for publication 18 September 2024
Published 15 January 2025

**Abstract**

The anode sheath of vacuum arc plasma plays a key role in the generation of anode plasma, but the effects of anode evaporation on the anode sheath remains unclear. In this paper, a theoretical model of a collisional sheath for multi-component plasma coupled with anode evaporation is developed, and the spatial evolution of the anode sheath at different anode surface temperatures is investigated. The results indicate that the distribution of charged particles density and potential in the anode sheath monotonically decreases in the absence or reduction of anode evaporation. When the anode surface temperature exceeds 1900 K, a potential hump appears within the sheath. This is due to enhanced anode evaporation increasing the metal vapor density, which intensifies electron impact ionization and charge exchange collisions, resulting in a higher net space charge density. Finally, the effects of various collision reactions and electron temperatures on the potential hump are analyzed. These findings are meaningful for understanding the anode plasma generation mechanism and regulating the anode plasma parameters.

Supplementary material for this article is available online

Keywords: vacuum arc plasma, anode evaporation, anode sheath, potential hump

## 1. Introduction

The anode vacuum arc ion sources [1, 2] can eliminate the impact of microparticles in plasma, and are widely used in advanced technologies such as ion accelerators and plasma thrusters [3–6]. The anode sheath plays a crucial role in the mass and heat transfer processes involved in generating anode plasma [7–13]. Therefore, a detailed study of the anode sheath characteristics is essential to understand the anode vacuum arc mechanism and to optimize the performance of the relevant equipment.

In terms of theoretical studies, previous researchers have calculated the potential distribution within the one-dimensional sheath by combining the Boltzmann approximation for electron and ion flux continuity [14–16], or employing the collisionless Langmuir formula [17–19]. However, the collisionless sheath model is unable to precisely portray the anode sheath's physical processes [20], and the Langmuir formula is inadequate for supersonic vacuum arc plasma sheath [21–23]. Shmelev *et al* [24, 25] modified the Langmuir formula by including Coulomb collision, and derived an anode sheath potential drop for supersonic plasma. However, lacking

* Authors to whom any correspondence should be addressed.

anode evaporation and ionization processes still limits the evolution of the anode sheath during anode vacuum arc plasma discharge.

Numerical simulations have also been used extensively to study the anode sheath such as magnetohydrodynamic (MHD) [26, 27], kinetic [28] and particle-in-cell (PIC) methods [29, 30]. Sun *et al* [31] employed an anode sheath coupled with MHD arc column model to study the physical process in the near-anode region. Wang *et al* [32] also established an MHD method and considered the anodic evaporation process. But the assumption of collisionless sheath in these studies cannot capture the kinetic behavior of the anode sheath [31–34]. Benilov and Benilova [28] developed a kinetic model for the cathode sheath considering electrode evaporation and ionization processes, which demonstrated the existence of a double space charge sheath with a potential hump near the cathode, while overlooking kinetic energy losses from ionization within the sheath. Tian *et al* [35] analyzed a collisionless anode sheath using a PIC method. Based on this, Wang *et al* [36] employed the same PIC method to consider the processes of anode evaporation, ionization, and others, revealing the characteristics of the anode sheath, but the discharge state of the anode vacuum arc cannot be fully represented by the effect of anode evaporation flux on the anode sheath was not analyzed in detail in these simulations.

Although previous studies have proved some explanations on the physical processes within the anode sheath, the effects of anode evaporation on distribution of anode sheath potential remain unclear. Bacon and Watts [37] observed in experiments that under conditions of strong evaporation, a potential hump occurs near the anode. However, its causes and influencing factors remain unexplained. Therefore, this paper proposes a theoretical model that integrates multi-component and multi-collision processes, to explore the impacts of anode evaporation on the characteristics of the vacuum arc plasma anode sheath.

The structure of the paper is as follows. Section 2 introduces the theoretical model. Section 3 describes the effects of different anode surface temperatures on the density of charged particles, ion velocities, and electric potential. The formation mechanism of the anode sheath potential hump and the influencing factors were also analyzed. Section 4 provides the conclusion.

## 2. Theoretical model and basic equations

Figure 1(a) shows a schematic diagram of the potential distribution between cathode and anode. For a Cu surface, the cathode is grounded, and the typical arc voltage is about 25 V [20]. The background gas pressure of $10^{-4}$ Pa in a vacuum environment. Depending on the electric potential distribution, the near-anode region can be divided into two parts: the plasma region and the anode sheath region, which gives the simulation model shown in figure 1(b). Compared to the potential distribution of the whole vacuum arc discharge, the variation of the potential in the near-anode region is smaller, about a few volts, whereas this paper focuses on the potential distribution in the near-anode region. Hence, the potential on the boundary of plasma is fixed at 0 V, the anode potential $\varphi_a$ is −4 V [25]. The ion incidence velocities in the near-anode region are presented in table 1. Furthermore, the position of the between the pre-sheath/sheath boundary can be determined self-consistently through the model. The ion incidence velocities in the near-anode region are presented in table 1. Furthermore, the position of the between the pre-sheath/sheath boundary can be determined self-consistently through the model. Copper metal is used for both cathode and anode. The cathode plasma, contains ions in various charge states, such as $Cu^{+}$, $Cu^{2+}$, $Cu^{3+}$, which expands at supersonic speed ($\sim 10^4$ m $s^{-1}$ ) toward the anode [33, 38, 39]. The multi-component cathode plasma traverses the anode sheath to heat the anode to vaporize material. Anode evaporation leads to various collision reactions within the anode sheath, such as ionization collisions between electrons and neutral (e–n collisions) and charge exchange collisions between ions and neutral (i–n collisions). The above collision reaction also exerts an influence on the Coulomb collisions between electrons and ions (e–i collisions) [36].

### 2.1. Evaporation model

It is assumed that the evaporation process at the anode surface is the primary mechanism for generating metal vapor, to be calculated as follows [28]:

$$n_a = \frac{P_{Cu}}{2kT_a} \tag{1}$$

here, $T_a$ is the anode surface temperature. The saturated vapor pressure $P_{Cu}$ of the evaporation copper at temperature $T_a$ can be calculated as follows [33, 34]:

$$P_{Cu} = \begin{cases} 133.33 \times 10^{-17650/T_a+13.39} \times T_a^{-1.25}, T_a \geqslant T_m \\ 133.33 \times 10^{-17870/T_a+10.63-1.6\times10^{-4}\times T_a} \times T_a^{-0.236}, T_a < T_m \end{cases} \tag{2}$$

$T_m = 1356$ K is the melting point of copper anode. As shown in figure 2, an increase in the anode surface temperature results in an increase in the vapor density. The radiation loses is much smaller compared with the heat flux density. Therefore, the energy loss by radiation is neglected in the paper [1].

In addition, the relationship between anode evaporation and anode surface temperature needs to be discussed. Dhamale *et al* [40] showed that during the anode evaporation process, the evaporated species notably impact arc properties, such as electrical conductivity, leading to a decrease in arc potential and subsequently reduction in the anode surface temperatures. However, Huang *et al* [41] showed that positive feedback between anode surface temperature and the anode evaporation process at copper anode surface temperature lower than 2706 K. Hence, when the anode surface temperature is relatively low, it is assumed in this paper that a stronger

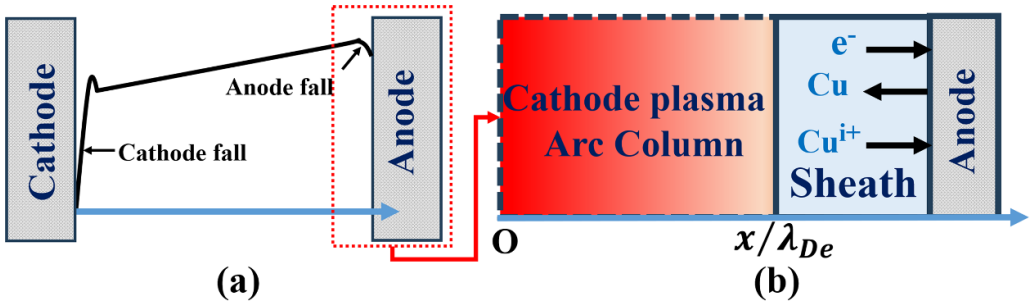


**Figure 1.** Schematic of (a) the potential distribution between cathode and anode and (b) the simulation model.

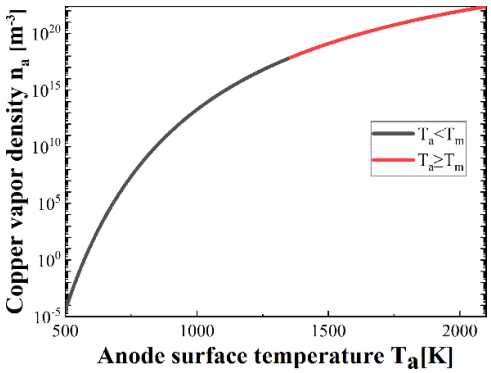


**Figure 2.** Relationship between the anode surface temperature and the copper vapor density.

anode evaporation process leads to a higher anode surface temperature, resulting in a higher density of copper vapor, as illustrated in figure 2.

### 2.2. Model of the near-anode region

Under steady-state conditions, the uniform ionization source terms are accounted for throughout the domain [28, 42, 43], and the governing equations for each type of ion as follows equations (3) and (4).

The ion fluid continuity equation [44]:

$$\frac{\mathrm{d}}{\mathrm{d}x}(n_i v_i) = K_i n_\mathrm{e} \tag{3}$$

where $n_i, v_i, K_i$ are the density, velocity, and ionization frequency of the $i$th ion, respectively. $n_\mathrm{e}$ is the electron density.

The ion momentum equation [42, 43]

$$m_i v_i \frac{\mathrm{d}v_i}{\mathrm{d}x} = -Z_i \mathrm{e}\frac{\mathrm{d}\varphi}{\mathrm{d}x} - \frac{1}{n_i}\frac{\mathrm{d}p_i}{\mathrm{d}x} - \frac{\min_i v_i \upsilon_i}{n_i} - \frac{n_\mathrm{e}}{n_i} k_i m_i v_i + \gamma_i \frac{n_\mathrm{e}}{n_i} m_\mathrm{e} \upsilon_{\mathrm{e}i}(v_\mathrm{e} - v_i) \tag{4}$$

where $m_i, Z_i, p_i = n_i k_\mathrm{B} T_i, \upsilon_i$ are the mass, charge state, pressure and ion-neutral collision frequency of the $i$th ion species, respectively. $e = 1.6 \times 10^{-19}$ C is the elementary charge, $k_\mathrm{B} = 1.38 \times 10^{-23}$ J K$^{-1}$ is the Boltzmann constant. The right-hand side of equation (4) represents the electrostatic force term, ion pressure gradient term, as well as the momentum transfer due to i–n collisions, e–n collisions, e–i collisions, respectively. Neutral particles are considered as background.

Electron collision ionization frequency $K_i = \alpha_\mathrm{g} n_{i-1}$, $n_0$ is the neutral particle density (or expressed as metal vapor density), $\alpha_\mathrm{g}$ is the ionization rate coefficient [33, 34, 38, 45]:

$$\alpha_\mathrm{g} = C k_\mathrm{B} T_\mathrm{e} \sqrt{\frac{8 k_\mathrm{B} T_\mathrm{e}}{\pi m_\mathrm{e}}} \left(\frac{I_\mathrm{g}}{k_\mathrm{B} T_\mathrm{e}} + 2\right) \exp\left(-I_\mathrm{g} / k_\mathrm{B} T_\mathrm{e}\right) \tag{5}$$

here, for singly charged copper ion ionization : $C = 2.6 \times 10^{-21} \mathrm{m}^2/\mathrm{eV}^{-1}$, for other types of ions, $C = 2.6 \times 10^{-21} (\frac{I_\mathrm{H}}{I_\mathrm{g}}) \mathrm{m}^2/\mathrm{eV}^{-1}$, $I_\mathrm{H} = 13.6$ eV is the ionization potential of a hydrogen atom. $I_\mathrm{g}$ is the ionization potential of species g, which mean that electron need of 7.72 eV for the $\mathrm{Cu} \rightarrow \mathrm{Cu}^+$, 20.29 eV for $\mathrm{Cu}^+ \rightarrow \mathrm{Cu}^{2+}$, and 36.84 eV for $\mathrm{Cu}^{2+} \rightarrow \mathrm{Cu}^{3+}$. $\gamma$ is Braginskii coefficient [38], their values are 0.513 in the case of $Z_1 = 1$, 0.441 in the case of $Z_2 = 2$, and 0.397 in the case of $Z_3 = 3$. $\upsilon_{ei}$ is the collision frequency of the electron with the $i$th ion [38, 39].

$$\upsilon_{\mathrm{e}i} = \frac{Z_i^2 n_i (\ln\Lambda / 10)}{3.5 \times 10^{10} \left(T_\mathrm{e}[\mathrm{eV}]^{3/2}\right)} \tag{6}$$

$\ln\Lambda$ is the Coulomb logarithm.

The distribution of plasma electron is Maxwellian with density obeying the Boltzmann distribution.

$$n_\mathrm{e} = n_{\mathrm{e}0} \exp\left(\frac{\mathrm{e}\varphi}{k T_\mathrm{e}}\right). \tag{7}$$

The system of equations is closed by Poisson's equation.

$$\frac{\mathrm{d}^2\varphi}{\mathrm{d}x^2} = -\frac{e}{\varepsilon_0}\left(\sum_{i=1}^{3} Z_i n_i - n_\mathrm{e}\right). \tag{8}$$

The quasi-neutrality condition imposed at the simulation domain $X = 0$:

$$\sum_{i=1}^{3} Z_i n_{0i} = n_{0\mathrm{e}}. \tag{9}$$

The dimensionless variables are introduced into the above equations to simplicity calculation [46–50]:

$$\phi = \frac{-e\varphi}{k_B T_e}, N_e = \frac{n_e}{n_0 e}, Ni = \frac{ni}{n_0 e}, X = \frac{x}{\lambda_{De}}, u_i = \frac{v_i}{c_{s1}}, u_e = \frac{v_e}{c_s 1}, \tau_i = \frac{T_i}{T_e} \quad (10)$$

here, $\lambda_{De} = (\varepsilon 0 k_B T_e / e^2 n_0 e)^{1/2}$ is the Debye length. The ions velocity is dimensionless with reference to the Bohm velocity $c_{s1} = (k_B T_e / m_1)$ of the $Cu^+$ ion. Substituting the variables (10) into (3), (4), and (7)–(9) yields a set of dimensionless differential equations:

$$\frac{d}{dX}(N_i u_i) = K_i N_e \quad (11)$$

$$\left(1 - \frac{\tau_1}{u_1^2}\right) u_1 \frac{d_u 1}{dX} = Z_1 \frac{d\phi}{dX} - K_1 \frac{\tau_1}{u_1}\left(\frac{N_e}{N_1}\right) - K_1 u_1 \left(\frac{N_e}{N_1}\right) - \chi_1 u_i^2 + \gamma 1 \frac{(N_{0e} u_0 e - N_e u_1)}{N_1} H_1 \beta \quad (12)$$

$$\left(1 - \mu_1 \frac{\tau_2}{u_2^2}\right) u_2 \frac{du_2}{dX} = Z_2 \mu_1 \frac{d\phi}{dX} - K_2 \mu_1 \frac{\tau_2}{u_2}\left(\frac{N_e}{N_2}\right) - K_2 u_2 \left(\frac{N_e}{N_2}\right) - \chi_2 u 2^2 + \gamma_2 \mu_2 \frac{(N_0 e u_0 e - N_e u_3)}{N3} H_2 \beta \quad (13)$$

$$\left(1 - \mu_2 \frac{\tau_3}{u_3^2}\right) u_3 \frac{du_3}{dX} = Z_3 \mu_2 \frac{d\phi}{dX} - K_3 \mu_2 \frac{\tau_3}{u_3}\left(\frac{N_e}{N_3}\right) - K_3 u_3 \left(\frac{N_e}{N3}\right) - \chi_3 u_3^2 + \gamma_3 \mu_2 \frac{(N_0 e u_0 e - N_e u_3)}{N_3} H_3 \beta \quad (14)$$

$$\frac{d^2\phi}{dX^2} = Z_1 N_1 + Z_2 N_2 + Z_3 N_3 - \exp(-\phi) \quad (15)$$

here, $\mu_1 = m_1/m_2$, $\mu_2 = m_1/m_3$. $\lambda_i = c_{s1}/k_i$ is the mean free path of electron impact ionization. $K_i = \lambda_{De}/\lambda_i$. $\chi_i = n_a \sigma_{si} \lambda_{De}$ ($i = 1, 2, 3$ corresponding $Cu^+$, $Cu^{2+}$, $Cu^{3+}$) is a dimensionless parameter for the frequency of i–n collisions. $u_0 e = v_0 e / c_s 1$, $N_0 e = n_0 e / n_0 e$, $\beta = m_e / m_1$, $H_i = \lambda_{De} / \lambda_e i$. $\lambda_{ei} = c_s 1 / \upsilon ei$ is the mean free path of e-i collisions. Further details on the physical models that consider other collisions can be found in the supplementary material.

The boundary conditions are set as: $N_i(X = 0) = N_{0i}$, $u_i(X = 0) = u_{0i}$, $d\phi / dX(X = 0) = 0$, $\phi(X = 0) = 0$, $\phi(X = X_a) = \phi_a = -e\varphi_a / k_{Te}$. Ions in different charge states within a plasma exhibit identical density and temperature, and the electron density obtained through the quasi-neutrality relationship. Assuming ions in different charge states possess identical incident velocities [38], with the ion initial velocities of $Cu^+$, $Cu^{2+}$, and $Cu^{3+}$ set are $1.6 \times 10^4 m\ s^{-1}$ . In previous studies, the electron velocity was found to be larger than the ion velocity by about an order of magnitude, with the electron velocity set at $10^5 m\ s^{-1}$, and the electron temperature at 3 eV [45]. The specific values used for the simulation are given in table 1.

**Table 1.** Physical parameters at the plasma boundary of the theoretical model.

| Species | $Cu^+$ | $Cu^{2+}$ | $Cu^{3+}$ | $e^-$ |
|---|---|---|---|---|
| $T$ (eV) | 1.0 | 1.0 | 1.0 | 3.0 |
| $v_i$ ($m\ s^{-1}$) | $1.6 \times 10^4$ | $1.6 \times 10^4$ | $1.6 \times 10^4$ | $1.0 \times 10^5$ |
| $n_i$ ($m^{-3}$) | $10^{20}$ | $10^{20}$ | $10^{20}$ | $6 \times 10^{20}$ |

## 3. Result and discussion

### 3.1. Effects of anode surface temperature on the density, velocity of particle and electric potential

Figure 3 shows the variation of charged particle density, and ions velocity in the near-anode region. It is noteworthy that the statistics of ions encompass both the incident ions and the newly generated ions resulting from ionization. At anode surface temperature of 1200 K, the density of ions and electron decreases with spatial position since the ions are accelerated in the anode sheath mainly by e–i collisions and electric field force. As the anode surface temperature increases to 2047 K, the charged particles density increases and then decreases with spatial position, while the ions velocity exhibits an opposite trend. This phenomenon is attributed to the increased anode surface temperature, which raises the metal vapor density and intensify the frequency of e–n and i–n collisions. Consequently, the ions were slowed down and the charged particles density increased. When the electric field force exceeds the e–n and i–n collisions, the ion accelerates, leading to decrease in ions density.

The electric potential distribution ($\varphi$) under different anode surface temperature are given in figure 4. When the anode surface temperature is below 1900 K, the sheath potential gradually decreases with spatial position [35, 36]. When the anode surface temperature reaches over 1900 K, a potential hump occurs. In prior research, Schuocker [51], Leffort [52] and Londer [53] had also indicated the presence of a potential hump near the anode. Specifically, Ecker [54] suggested that the potential hump is approximately 1 V, which is much lower than measured experimentally [37]. In this study as the anode surface temperature reaching to 2000 K, the potential hump equals 1 V, and the higher anode surface temperature the higher potential hump.

### 3.2. Factors influencing the potential hump

Schematic diagrams of electron density, ion density and ion velocity under strong anode evaporation are shown in figure 5. Previously, Ecker [54] attributed the potential hump near the anode to collision energy loss. As shown in figure 3, when the anode surface temperature reaches 2047 K, the density of $Cu^+$ ions increase significantly, while the other ion's density are relatively small. According to ion momentum equation (4), the loss of $Cu^+$ ion kinetic energy at different position is counted.

$$\frac{dE_i}{dx} = -Z_{ie}\frac{d\varphi}{dx} - \frac{kT_i}{n_i}\frac{dn_i}{dx} + R_{coll} \quad (16)$$

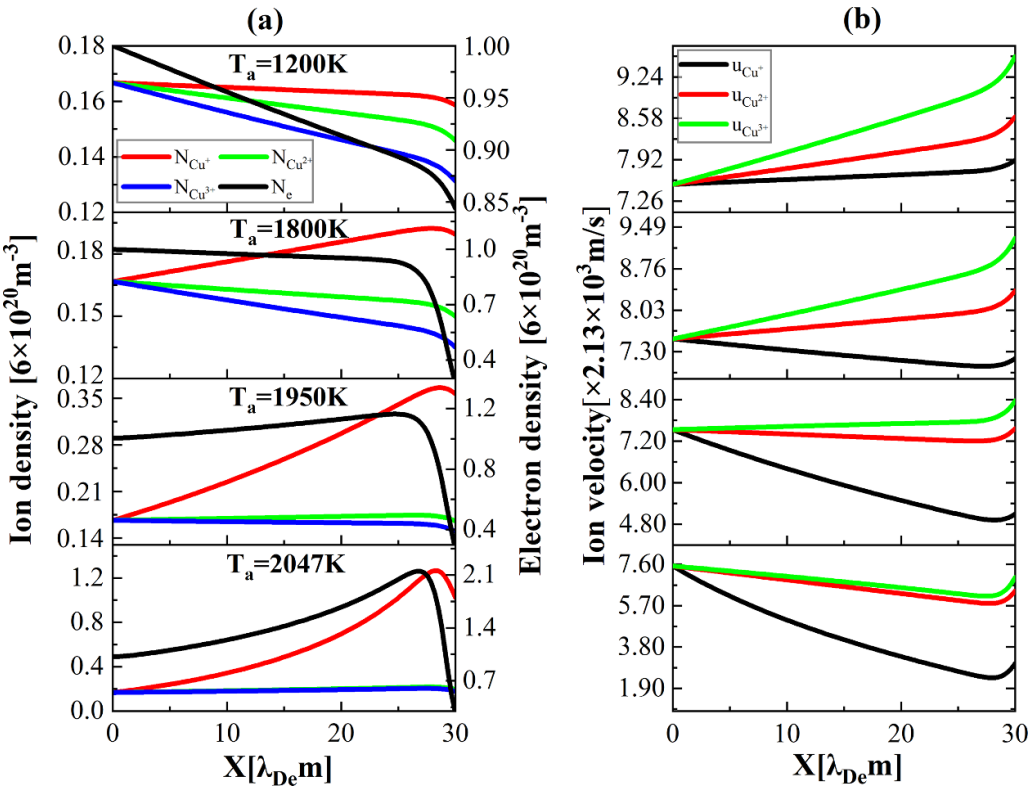


**Figure 3.** Spatial distribution of (a) charged particle density and (b) ion velocities in the near-anode region at different anode surface temperature.

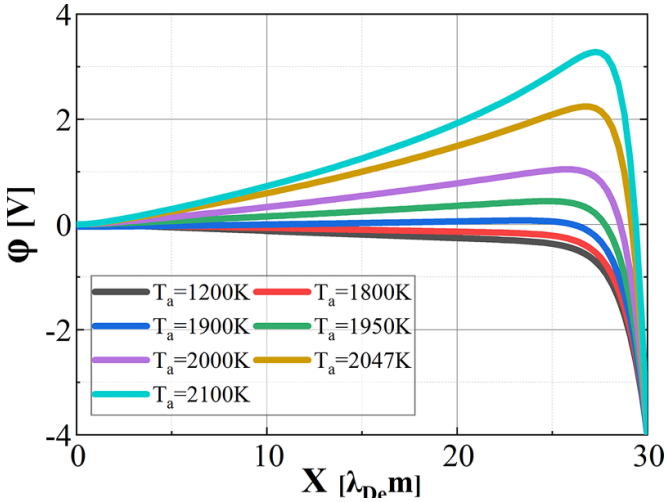


**Figure 4.** Variation of the electric potential ($\varphi$) with spatial position in the near-anode region at different anode surface temperature.

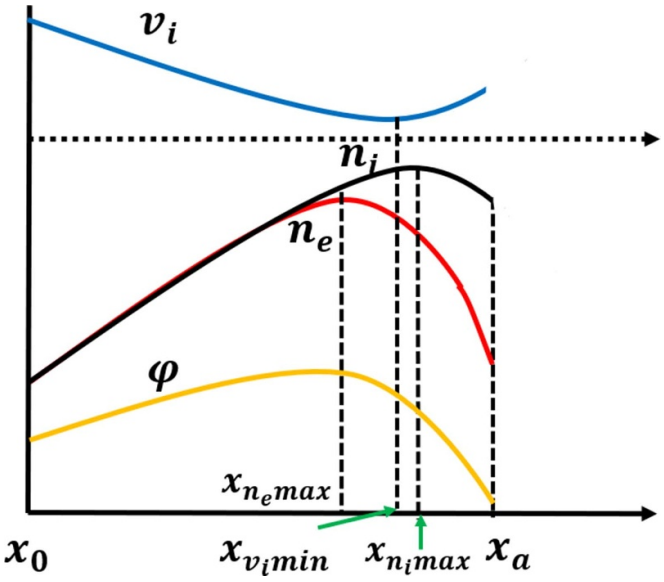


**Figure 5.** Schematic diagrams of ion velocity, charged particle density and electric potential in the near-anode region.

where $R_{\text{coll}}$ denotes the sum of momentum transfer for i–n collisions, e–n collisions and e–i collisions.

Integrating both sides of equation (16) by multiplying d$x$ gives the following equation:

$$\Delta E_i = -Z_{ie}\Delta\varphi - kT_i \ln\left(n_i/n_i 0\right) + \Delta E_{\text{coll}} \qquad (17)$$

where, $\Delta E_{\text{coll}}$ is the $Cu^+$ ion kinetic energy loss term due to collisions.

In table 2, form $x_0$ to $x_{ne\max}$, the electric field force term, collision terms, and pressure gradient term perform negative work, decelerating ions while increasing their density. From $xn_e$ max to $x_{vi\min}$, the electric field force performs positive work, while the collision term and pressure gradient term perform negative work, leading to a continuous decrease in ion velocity due to the weaker electric field force, and an increase

**Table 2.** $Cu^+$ ion kinetic energy loss at different positions ($x_0, x_{ne\,\max}, x_{vi\,\min}, x_{ni\,\max}, x_a$ are the positions of the $X = 0$, the density peaks of electron and ions, position of the ion velocity minimum, and anode, respective.).

| Type | Position | $\Delta E_i$ | $-Z_i e\Delta\varphi$ | $-kT_i\mathrm{In}(n_i/n_i0)$ | $\Delta E_{\mathrm{coll}}$ |
|---|---|---|---|---|---|
| Three collisions | $x_0 \rightarrow x_{ne\,\max}$ | −76.075 eV | −2.313 eV | −1.969 eV | −71.793 eV |
| | $x_0 \rightarrow x_{ni\,\max}$ | −76.596 eV | −1.679 eV | −2.035 eV | −72.882 eV |
| | $x_{ne\,\max} \rightarrow x_{vi\,\min}$ | −0.659 eV | 0.217 eV | −0.074 eV | −0.802 eV |
| | $x_{vi\,\min} \rightarrow x_{ni\,\max}$ | 0.020 eV | 0.204 eV | −0.007 eV | −0.177 eV |
| | $x_{ne\,\max} \rightarrow x_a$ | 4.251 eV | 6.030 eV | 0.128 eV | −1.907 eV |

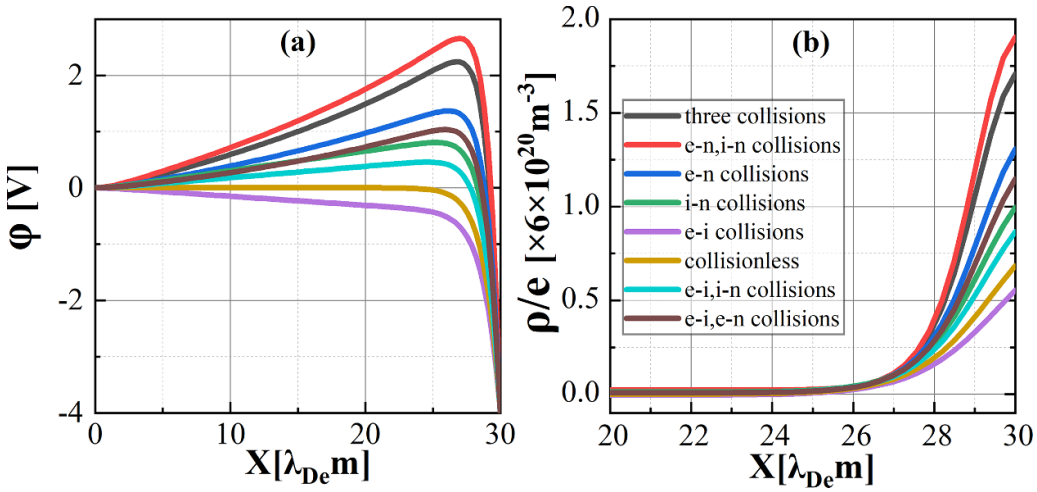


**Figure 6.** Variation of (a) the electric potential ($\varphi$) and (b) the net space charge density versus the spatial position for different collision reactions in the near-anode region. Condition: $T_a = 2047$ K, $T_e = 3$ eV.

in ion density. Thus, $xn_e\,\max$ represents the position where the electric field is zero, corresponding to the potential hump, where the electron density reaches its maximum. At $x_{vi\,\min}$, the three forces reach equilibrium, where the ion velocity reaches its minimum. Form $x_{vi\,\min}$ to $x_{ni\,\max}$, the electric field force is greater than the other terms and the ion velocity increases, the ion density continues to increase due to the ionization process. From $x_{ni\,\max}$ to $x_a$, the electric field force exceeds other terms, accelerating ions, the pressure gradient performs positive work, resulting in a decrease in ion density. The peak position of the ion density was found to be where the loss of ion kinetic energy due to collisions is greatest, rather than the peak position of electron density. Therefore, the potential hump cannot be precisely described using collision energy loss, and net space charge density may provide a better explanation.

*3.2.1. Different collision reactions.* The effects of different collision reactions on the electric potential distribution and net space charge density ($\rho/e = [\sum_{i=1}^{3} Z_i n_i - n_e]/n_0 e$) are compared in figure 6. The anode surface temperature reaches 2047 K, the magnitude of the net space charge density between the various collision reactions is as follows: $\rho_{(en,in)} > \rho_{(three)} > \rho_{(en)} > \rho_{(en,ei)} > \rho_{(in)} > \rho_{(in,ei)} > \rho_{(collisionless)} > \rho_{(ei)}$, the mean free paths for various collisions are as follows: e–i ($\sim 1.1 \times 10^{-8}$ m), e–n ($\sim 1.2 \times 10^{-5}$ m), i–n ($\sim 7.1 \times 10^{-6}$ m), and the Debye length ($\sim 5.3 \times 10^{-7}$ m). The e–i collisions result in the transfer of kinetic energy from electron to ions, increasing the ions velocity. According to the continuity equation, the ions density will decrease, and thus lower the net space charge density. Therefore, Coulomb collisions in the anode sheath cannot be neglected, which is consistent with Shmelev *et al* [24, 25]. In conditions of strong evaporation, the increase in vapor density leads to a decrease in the mean free path of i–n collisions, resulting in a stronger collision frequency. As ions transfer part of their energy to atoms and decelerate, causing an increase in ion density and the net space charge density. Meanwhile, the increased vapor density reduces the mean free path of e–n collisions and enhances the e–n collisions frequency, producing electron and ions, increasing the net space charge density. Therefore, charge exchange collisions and electron impact ionization are crucial factors contributing to the increase in net space charge density. According to Poisson's equation, increasing the net space charge density in the anode sheath raises the height of the potential hump. In the case of strong anode evaporation, the use of a collisionless sheath cannot precisely describe the anode sheath. A comprehensive consideration of the above three collision reactions offers deeper insights into the physical properties of the anode sheath.

*3.2.2. Different electron temperature.* Figure 7 shows the effects of different electron temperatures on the electric potential and net space charge density of the near-anode region. As shown in figure 7(a), the electron temperature is 4 eV and the potential hump reaches 5.92 V. According to

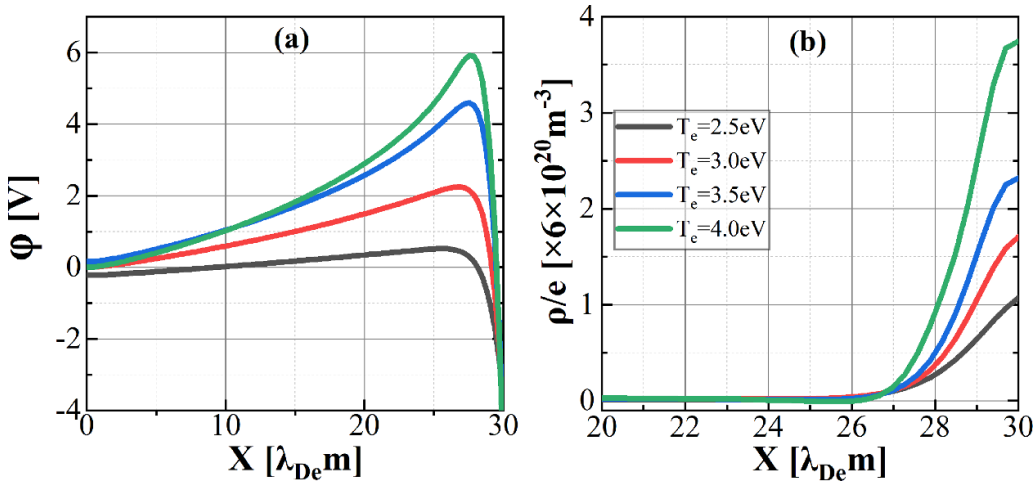


**Figure 7.** Variation of (a) the electric potential ($\varphi$) and (b) the net space charge density versus the spatial position for electron temperature in the near-anode region. Condition: $T_a = 2047$ K, three collision reactions.

equation (5), the increase in electron temperature enlarges the e-n collisions rate coefficient, which raises the electron and ions density due to ionization collision, the net space charge density increases, leading to a shift in anode sheath potential hump. Thus, the height of the potential hump rises with the increase in electron temperature.

## 4. Conclusions

In this paper, a theoretical model is developed to investigate the effects of anode evaporation on anode sheath characteristics.

(1) In a vacuum discharge, an anode sheath is formed between the arc column and the anode surface. At anode surface temperatures in excess of 1900 K, the e–n and i–n collisions are gradually enhanced, the net space charge density in the anode sheath increases, resulting in a potential hump occurs in the anode sheath.
(2) Combined consideration of e–n and i–n collision reactions causes the net charge density in the anode sheath to increase, resulting in an increase in the height of the potential hump. An increase in electron temperature causes an increase in the ionization rate coefficient, leading to an increase in the potential hump. Exploring these factors will be essential for gaining a comprehensive understanding of how anode evaporation influences anode sheath characteristics and the subsequent formation of potential humps.

## Data availability statement

All data that support the findings of this study are included within the article (and any supplementary files).

## Acknowledgment

This work is partially supported by PFCAEP project No. YZJJZQ2022016, and NSFC project No. 12375246.

## ORCID iDs

Zhaohui Liu https://orcid.org/0000-0001-7602-0065
Mengmeng Song https://orcid.org/0000-0003-1363-1330
Wei Yang https://orcid.org/0000-0003-0114-0403
Ye Dong https://orcid.org/0000-0003-4662-5623
Qiang Sun https://orcid.org/0000-0002-2617-2578

## References

[1] Boxman R L, Sanders D and Martin P J 1996 *Handbook of Vacuum Arc Science & Technology: Fundamentals and Applications* (William Andrew)
[2] Musa G, Ehrich H and Mausbach M 1994 *J. Vac. Sci. Technol.* A **12** 2887–95
[3] Brown I and Oks E 2005 *IEEE Trans. Plasma Sci.* **33** 1931–43
[4] Nikolaev A G 2019 *IEEE Trans. Plasma Sci.* **47** 3590–3
[5] Efim O and Ian B 2004 *The Physics and Technology of Ion Sources* 2nd edn (Wiley)
[6] Brown I G, Galvin J E and MacGill R A 1985 *Appl. Phys. Lett.* **47** 358–60
[7] Zhang Z, Ma H, Yi X, Liu Z, Geng Y and Wang J 2017 Study on the heat flux density delivered to the anode at the transition to anode spot formation in high current vaccum arcs *2017 4th Int. Conf. on Electric Power Equipment-Swithing Technology (Xi'an, China)*
[8] Tian Y, Wang Z, Zhou Z, Geng Y and Liu Z 2014 A coupled simulation model of the heating process on an anode under high-current vacuum arcs *26th Int. Symp. on Discharges and Electrical Insulation in Vacuum* (*Mumbai India*)
[9] Wang L, Zhou X, Wang H, Qian Z, Jia S, Yang D and Shi Z 2012 *IEEE Trans. Plasma Sci.* **40** 2237–46
[10] Wang L, Jia S, Liu Y, Chen B, Yang D and Shi Z 2010 *J. Appl. Phys.* **107** 113306

[11] Rosenthal H, Beilis I, Goldsmith S and Boxman R L 1994 *Proc. SPIE* vol **2259** pp 164–9
[12] Ehrich H 1988 *J. Vac. Sci. Technol.* A **6** 134–8
[13] Ehrich H, Hasse B, Müller K G and Schmidt R 1988 *J. Vac. Sci. Technol.* A **6** 2499–503
[14] Boxman R L and Goldsmith S 1983 *J. Appl. Phys.* **54** 592–602
[15] Cunha M D, Kaufmann H T C, Benilov M S, Hartmann W and Wenzel N 2017 *IEEE Trans. Plasma Sci.* **45** 2060–9
[16] Kaufmann H T C, Cunha M D, Benilov M S, Hartmann W and Wenzel N 2017 *J. Appl. Phys.* **122** 2060–9
[17] Lieberman M A and Lichtenberg A 2005 *Principles of Plasma Discharges and Materials Processing* 2nd edn (Wiley)
[18] Schade E and Shmelev D L 2003 *IEEE Trans. Plasma Sci.* **31** 890–901
[19] Wang L, Jia S, Shi Z and Rong M 2005 *J. Phys. D: Appl. Phys.* **38** 1034–41
[20] Shmelev D L 2013 *IEEE Trans. Plasma Sci.* **41** 1969–73
[21] Londer Y I and Ulyanov K N 2013 *Plasma Phys. Rep.* **39** 849–56
[22] Londer Y I and Ulyanov K N 2013 *IEEE Trans. Plasma Sci.* **41** 2002–6
[23] Tonks L and Langmuir I 1929 *Phys. Rev.* **34** 876–922
[24] Shmelev D L, Barengolts S A and Tsventoukh M M 2014 *Plasma Sources Sci. Technol.* **23** 062004
[25] Shmelev D L, Barengolts S A and Tsventoukh M M 2014 On the negative anode voltage fall of high-current vacuum arc: PIC-modelling results *26th Int. Symp. on Discharges and Electrical Insulation in Vacuum* (*Mumbai India*)
[26] Meng X, Wang Y and Ma T 2000 *J. Appl. Phys.* **88** 40–43
[27] Hatami M M, Shokri B and Niknam A R 2009 *J. Phys. D: Appl. Phys.* **42** 025204
[28] Benilov M S and Benilova L G 2010 *J. Phys. D: Appl. Phys.* **43** 345204
[29] Taccogna F, Longo S and Capitelli M 2004 *Phys. Plasmas* **11** 1220–8
[30] Gyergyek T, Jurcic-Zlobec B and Cercek M 2008 *Phys. Plasmas* **15** 063501
[31] Sun Q, Wang C, Zhan Z, Chen X, Qin P and Xia W 2019 *J. Phys. D: Appl. Phys.* **52** 265204
[32] Wang L, Huang X, Jia S, Deng J, Qian Z, Shi Z, Schellenkens H and Godechot X 2015 *J. Appl. Phys.* **117** 243301
[33] Zhang Z, Wang L, Yang Z, Luo M and Li J 2022 *Plasma Sci. Technol.* **24** 044002
[34] Wang L, Huang X, Zhang X and Jia S 2017 *J. Phys. D: Appl. Phys.* **50** 095203
[35] Tian Y, Zhou Z, Wang Z, Geng Y, Wang J and Liu Z 2015 Kinetic numerical simulation of anode sheath of vacuum arcs *2015 3rd Int. Conf. on Electric Power Equipment—Switching Technology (ICEPE-ST)* (*Busan Korea*)
[36] Wang Z, Zhou Z, Tian Y, Wang H, Wang J, Geng Y and Liu Z 2017 *J. Phys. D: Appl. Phys.* **50** 295203
[37] Bacon F M and Watts H A 1975 *J. Appl. Phys.* **46** 4758–66
[38] Sun Q, Yang W and Zhou Q 2020 *J. Phys. D: Appl. Phys.* **53** 375201
[39] Sun Q, Zhou Q, Zhang H, Yang W, Dong Y and Song M 2022 *Plasma Sources Sci. Technol.* **31** 015014
[40] Dhamale G D, Das S, Murphy A B, Kandada S P R, Balasubramanian C and Ghorui S 2022 *J. Phys. D: Appl. Phys.* **55** 375203
[41] Huang X, Wang L, Jia S, Qian Z, Deng J and Shi Z 2015 *IEEE Trans. Plasma Sci.* **43** 2283–93
[42] M S B 2010 *J. Phys. D: Appl. Phys.* **43** 175203
[43] Moulick R, Garg A and Kumar M 2021 *Contrib. Plasma Phys.* **61** e202100047
[44] Hatami M M and Kourakis I 2022 *Sci. Rep.* **12** 6905
[45] Sun Q, Yang W and Zhou Q 2020 *Phys. Plasmas* **27** 053501
[46] Franklin R N 2003 *J. Phys. D: Appl. Phys.* **36** 1806–9
[47] Franklin R N 2000 *J. Phys. D: Appl. Phys.* **33** 3186–9
[48] Valentini H B and Herrmann F 1996 *J. Phys. D: Appl. Phys.* **29** 1175–80
[49] Riemann K U 1995 *IEEE Trans. Plasma Sci.* **23** 709–16
[50] Mahanta M K and Goswami K S 2000 *Pramana.* **56** 579–84
[51] Schuocker D 1979 *IEEE Trans. Plasma Sci.* **7** 209–16
[52] Lefort A and Andanson P 1985 *IEEE Trans. Plasma Sci.* **PS-13** 296–9
[53] Londer Y I and Ulyanov K N 2014 *Plasma Phys. Rep.* **40** 312–21
[54] Ecker G 1974 *IEEE Trans. Plasma Sci.* **PS-2** 130–46